Available online at www.sciencedirect.com
SciVerse ScienceDirect
www.elsevier.com/locate/jmbbm

Mechanics of composite elasmoid fish scale assemblies and their bioinspired analogues

Ashley Browning[a], *Christine Ortiz*[b,*], *Mary C. Boyce*[a,*]

[a]*Department of Mechanical Engineering, 77 Massachusetts Ave, Massachusetts Institute of Technology, Cambridge, MA, USA*
[b]*Department of Materials Science and Engineering, 77 Massachusetts Ave, Massachusetts Institute of Technology, Cambridge, MA, USA*

ARTICLE INFO

Article history:
Received 28 July 2012
Received in revised form
5 November 2012
Accepted 11 November 2012
Available online 24 November 2012

Keywords:
Biomimetic
Composite
Natural armor
Fish scale

ABSTRACT

Inspired by the overlapping scales found on teleost fish, a new composite architecture explores the mechanics of materials to accommodate both flexibility and protection. These biological structures consist of overlapping mineralized plates embedded in a compliant tissue to form a natural flexible armor which protects underlying soft tissue and vital organs. Here, the functional performance of such armors is investigated, in which the composition, spatial arrangement, and morphometry of the scales provide locally tailored functionality. Fabricated macroscale prototypes and finite element based micromechanical models are employed to measure mechanical response to blunt and penetrating indentation loading. Deformation mechanisms of scale bending, scale rotation, tissue shear, and tissue constraint were found to govern the ability of the composite to protect the underlying substrate. These deformation mechanisms, the resistance to deformation, and the resulting work of deformation can all be tailored by structural parameters including architectural arrangement (angle of the scales, degree of scale overlap), composition (volume fraction of the scales), morphometry (aspect ratio of the scales), and material properties (tissue modulus and scale modulus). In addition, this network of armor serves to distribute the load of a predatory attack over a large area to mitigate stress concentrations. Mechanical characterization of such layered, segmented structures is fundamental to developing design principles for engineered protective systems and composites.

© 2013 Elsevier Ltd. All rights reserved.

1. Introduction

Fish scale assemblies provide a diversity of natural engineered designs which achieve multiple functionalities including mechanical protection, anisotropic flexibility, hydration, regeneration, repair, and camouflage (Arciszewski and Cornell, 2006; Colbert and Morales, 2001). Examples of design categories of fish scale assemblies include structure and composition of the individual scale (layering), morphometrics or shape of individual scales, composite design, inter-scale connections and joints, and scale assembly spatial arrangements (Garrano et al., 2012; Gemballa and Bartsch, 2002; Ibanez et al., 2009; Jawad and Al-Jufaili, 2007; Sire et al., 2009; Vernerey and Barthelat, 2010). This study focuses on "elasmoid" scale assemblies of teleost fish. Individual elasmoid scales are composed of a mineralized outer layer (16–59 vol%) of hydroxyapatite (Garrano et al., 2012; Torres et al., 2008; Whitear, 1986; Zhu et al., 2012) whose geometry is an ellipsoidal or rectangular plate with aspect ratios of 25–100. Elasmoid scales are imbricated (overlapping), non-articulating and embedded within a compliant non-mineralized tissue (Fig. 1), with varying scale aspect ratio, scale orientation angle, spatial overlap, and volume

*Corresponding authors.
E-mail addresses: cortiz@mit.edu (C. Ortiz), mcboyce@mit.edu (M.C. Boyce).

1751-6161/$ - see front matter © 2013 Elsevier Ltd. All rights reserved.
http://dx.doi.org/10.1016/j.jmbbm.2012.11.003

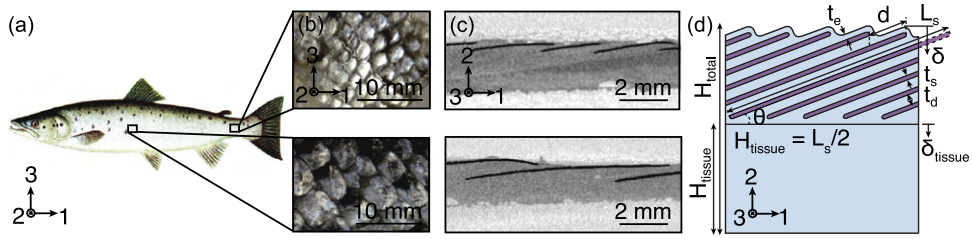

Fig. 1 – Overview of the structure of elasmoid fish scale assemblies. (a) Integument of a fresh Atlantic salmon (*Salmo salar*) obtained from a local fishery (New Deal Fish Market, Cambridge, MA). Image adapted from Östman, Elisabeth, Iduns kokbok, 1911, Web, Last accessed on May 1, 2012. http://commons.wikimedia.org/wiki/Salmo_salar, (b) overlapping scales and underlying tissue were excised from the main body and caudal peduncle (tail) near the lateral line and (c) micro-computed tomography (μCT) was employed to obtain two-dimensional slices (false coloring) of structure. Scans were performed and analyzed following our previously reported methods (Connors et al., 2012; Song et al., 2010). Scales are embedded in a dermal tissue at various geometric configurations, which are summarized (d).

fraction of scales, creating a robust composite system in which the interplay between the mineralized scales and the compliant tissue plays a governing role in tailoring and controlling mechanical behavior and deformation mechanisms. This composite structure varies not only across species, but also along the body of individual fish as found by histological sections (Hawkes, 1974; Park and Lee, 1988; Sire, 1990; United States Fish and Wildlife Service, 2010; Whitear, 1986).

Experimental measurements of mechanical properties of elasmoid scales have been limited to the macroscale mechanics of an individual scale resisting penetration by a sharp indenter or uniaxial tensile testing. Testing of scales in a hydrated state found the tensile strength to range between 22 and 65 MPa and the toughness to be ~1 MPa (Garrano et al., 2012; Ikoma et al., 2003; Meyers et al., 2012; Torres et al., 2008; Zhu et al., 2012). The multilayered elasmoid fish scale was found to localize penetration by promoting cross-like fracture patterns in the outer layer (Zhu et al., 2012). On a larger length scale, Vernerey and Barthelat (2010) introduced a two-dimensional mathematical model of overlapping fish scales where accommodation of bending is determined as a function of scale geometry and material properties. They found that a strain-stiffening behavior of the assembly with increasing scale overlap provides the ability to distribute deformation over a large area during bending.

In this paper, a three-dimensional elastic, composite model was formulated for the case of the mineralized scales fully embedded in a compliant hyperelastic organic tissue matrix. Loading under the physiologically relevant conditions of blunt trauma and indentation is simulated as a function of scale material properties, aspect ratio, scale orientation angle, spatial overlap, and volume fraction of scales. The simulations allow for identification of deformation mechanisms, including the roles of scale bending, tissue shear, and scale rotation as a function of scale geometry, and the quantification of back-deflection, work of deformation, and spatially heterogeneous stress fields. Macroscale synthetic models were constructed from an engineering thermoplastic and silicone rubber using a combination of three-dimensional printing and molding fabrication methods. The synthetic models were experimentally tested to measure the mechanical performance and to validate the model predictions. Mechanical behavior under blunt compressive loading was measured where digital image correlation (DIC) was used to measure the strain fields in the composite material. These experimental and numerical models yield detailed insights into the roles and the tradeoffs of the composite structure providing constraint, shear, and bending mechanisms to impart protection and flexibility.

2. Materials and methods

2.1. *Geometry of elasmoid fish scale assembly*

The primary features of the structure of mineralized scales embedded in a soft tissue are captured in a micromechanical model consisting of (1) an upper layer of relatively high modulus (E_s) scale of aspect ratio L_s/t_s oriented at angle θ and embedded in a low modulus (E_t) tissue, and (2) a soft (low modulus E_t) tissue substrate support (representing the underlying collagenous layer) as shown in Fig. 1(c,d).

Typical values for the scale thickness in teleost fish are on the order of t_s~0.1 mm, but reported values range from 44 μm to 1 mm, (Whitenack et al., 2010; Meyers et al., 2012). Typical scale lengths, L_s, range from 5 to 15 mm, but have been reported over 100 mm long (Francis, 1990; Garrano et al., 2012; Jawad and Al-Jufaili, 2007; Meyers et al., 2012; Torres et al., 2008; Zhu et al., 2012). Despite the large range of observed scale lengths and thicknesses, the geometry of the fish scale preserves an aspect ratio $R_a = L_s/t_s$ between 25 and 100 based on the available literature and measurements. The effect of various geometric parameters will be studied (as discussed later) but the scale will be held at constant aspect ratio of either R_a=50 or 100, which were taken as intermediate and maximum values, respectively.

The scales are initially oriented at angle θ relative to a compliant tissue support (Fig. 1d). Scales overlap each other such that a fraction of the scale is embedded beneath an adjacent scale. The length d is the exposed length of scale, while the remaining length ($L_s - d$) is embedded beneath another scale. This degree of imbrication, or overlap, $K_d = d/L_s$ is a measure for the spatial overlap defined by Burdak (1979), who measured K_d for 16 species of the Cyprinidae family of fish and found that values range from

$0.24 \leq K_d \leq 1$ depending on species and body location. Fish with highly overlapping, heavily armored skins such as the tench (*Tinca tinca*), have $K_d \sim 0$, whereas lightly scaled fish have $K_d \sim 1$, as is the case for undulating eel-like fish. The average number of scales in a cross section of the tissue is normalized by the number of scales in a section for the case of zero scale overlap. As this non-overlapping configuration has a K_d of unity (no overlap corresponds to one scale per section), the variable K_d^{-1} is effectively the average number of scales in a cross section. The overlap along the circumference was determined to be constant for all species studied by Burdak (1979). In most teleost fish species, the upper epidermis follows the contours of the scale pockets (Whitear, 1986), and hence, the irregularity of the surface topology increases as a function of K_d and θ. A variable of scale volume fraction, ϕ, can be calculated in terms of the thickness of the dermis between scales t_d, and scale thickness t_s, as $\phi = t_s/(t_s + t_d)$. This fraction ϕ represents the scale-to-tissue ratio in the upper, scaled layer and does not include the tissue support, as this bottom layer serves only to capture physiologically relevant deformations in the underlying integument. This bottom tissue layer is fixed at height $H_{tissue} = L_s/2$. Here, the scale volume fraction is reported as $\phi(K_d, \theta, R_a)$ as shown in Fig. 2(a), whereas previous models, neglecting a composite system, only consider alinear fraction $\phi \sim K_d^{-1}$. This study will vary geometric parameters as governed by the following relationship:

$$\phi = \frac{\tan^2\theta + 1}{K_d R_a \tan\theta}$$

An approximate biologically relevant range of $\phi(K_d, \theta, R_a)$ is shown in Fig. 2(a) based on the available histological sections and μCT scans (Guinan, 2012; Hawkes, 1974; Park and Lee, 1988; Sire, 1990; United States Fish and Wildlife Service, 2010; Whitear, 1986). This non-dimensional formulation allows for length-independent analysis of composite assemblies across a range of length scales. A table of all parameters used in study can be found in supplemental Table S1.

2.2. *Prototype fabrication and mechanical testing*

Macroscale synthetic prototypes were fabricated and tested to characterize a row of scales in an assortment of geometric architectures. A computer aided drawing package (SolidWorks, Dassault Systémes) was used to create models of the scales in a variety of geometric configurations (Fig. 2). Scale aspect ratio was kept constant at $R_a = 50$ and scale fraction ϕ was varied from 0 to 1 by parametrically varying overlap K_d (0.1, 0.3, 0.5, 0.7, 0.9) and scale angle θ (2.5°, 5°, 10°, 20°, 40°) for a total of 21 arrangements (Table 1).

These models were exported as stereolithography (.STL) files for three-dimensional printing using fused deposition modeling (Dimension BST 1200es, Stratasys). Parts were built with thermopolymer acrylonitrile butadiene styrene (ABS) with a layer thickness of 0.010 inches and a breakaway support. The resulting parts were placed in an acrylic frame and used as a mold for a translucent silicone rubber (Mold Max 10 T, Smooth-On). After the rubber cured, the ABS scales were permanently embedded in the silicone and the frame was removed. The final macroscale models had scale

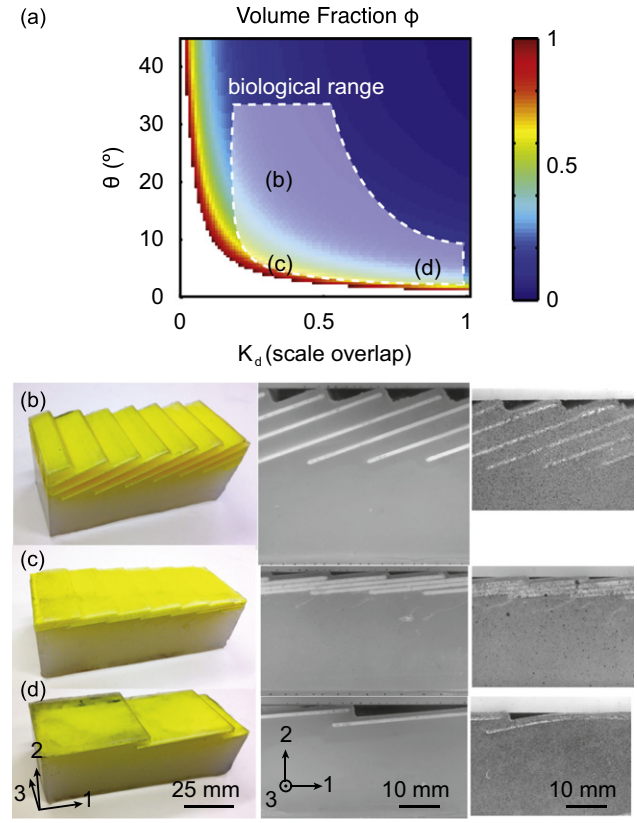

Fig. 2 – (a) Map of scale volume fraction ϕ and selected geometries for $R_a = 50$. Macroscale 3-D printed and molded synthetic fish scale inspired assembly of ABS (yellow) and silicone rubber (translucent) and images from digital image correlation (DIC) camera prior to loading (center) and deformed (right) for geometries: (b) $K_d = 0.3$, $\theta = 20°$, $\phi = 0.21$, (c) $K_d = 0.3$, $\theta = 5°$, $\phi = 0.77$ and (d) $K_d = 0.9$, $\theta = 5°$, $\phi = 0.26$. Selected configurations have similar scale overlap (b, c), angle (c, d), and volume fraction (b, d) to demonstrate the functional effect of each structural parameter. (For interpretation of the references to color in this figure caption, the reader is referred to the web version of this article.)

geometry $L_s = 50$ mm, $t_s = 1$ mm, were $100 \times 40 \times \sim 50$ mm in size, and contained 2–6 repeating scale units depending on angle θ and overlap K_d. Material properties of the silicone rubber and ABS were measured using compressive and tensile testing, respectively, and found the ABS to silicone rubber modulus ratio to be ~2000. These properties of elastic modulus (Table 2) are in the range of biological materials for wet elasmoid scales (Garrano et al., 2012; Lin et al., 2011; Torres et al., 2008) and fish tissue (Hebrank and Hebrank, 1986).

Plane strain compression testing of the synthetic prototypes was performed (Zwick Z2.5 kN, Zwick/Roel) at a loading rate of 0.1 mm/s to a maximum force of 400 N, corresponding to approximately 1.5–8.5 mm (equivalently 1.5–8.5 t_s) of compression depending on geometry. This macroscopic engineering stress $\sigma = F_2/A$ is calculated from the measured vertical reaction force, F_2, and the initial total sample cross-sectional (surface) area, A. To provide plane strain conditions for finite

Table 1 – Volume fractions ϕ for geometries studied where $R_a = 50$.

	ϕ	Overlap K_d				
		0.1	0.3	0.5	0.7	0.9
Angle θ	2.5°	–	–	0.92	0.66	0.51
	5°	–	0.77	0.46	0.33	0.26
	10°	–	0.39	0.23	0.17	0.13
	20°	0.62	0.21	0.12	0.09	0.07
	40°	0.41	0.14	0.08	0.06	0.05

Table 2 – Material parameters experimentally determined from synthetic prototype and employed in simulations.

Property	Scale	Tissue
Material	3-D printed ABS	Silicone rubber
Behavior	Elastic	Neo-Hookean
Modulus	$E_s = 880$ MPa	$E_{0,t} = 0.39$ MPa
Poisson's ratio	$\nu_s = 0.4$	$\nu_t \sim 0.49$

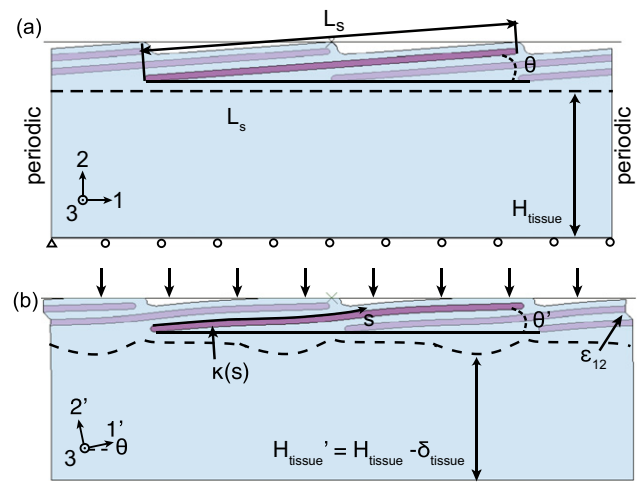

Fig. 3 – Deformation mechanisms under blunt loading with periodic boundary conditions. (a) Undeformed configuration and boundary conditions for $K_d = 0.5$, $\theta = 5$ deg, $\phi = 0.46$ and (b) deformed configuration exhibiting local scale curvature $\kappa(s)$, rotation $d\theta = \theta' - \theta$, shear strain ϵ_{12} in tissue, and back deflection δ_{tissue}.

thickness geometry, a frame was constructed with thick clear acrylic (PMMA) sheets, constraining the sample in the 3-direction, which was precisely adjusted to account for slightly varying sample thicknesses. Chalk powder and Teflon sheets were used to reduce friction on the sides and top/bottom of the rubber, respectively. A speckle pattern was applied on the samples with an airbrush and India ink for use with optical extensometry via digital image correlation (DIC). Images of the testing were taken at a rate of 1 fps (VicSnap, Correlated Solutions) and DIC (Vic-2D 2009, Correlated Solutions) was used to track global deformation and obtain local contours of logarithmic (Hencky) strain. Engineering strain ϵ is calculated as the total vertical displacement from DIC, δ, normalized by the initial total height, H_{total}. Shear strain is reported as engineering shear strain. Data from the digital extensometer were then synchronized to mechanical testing data to obtain engineering stress–strain curves. Back deflection δ_{tissue} is defined as deflection in the underlying tissue and corresponds to the change in height of the tissue layer H_{tissue}, as shown in Fig. 3. Back deflections are reported at depth t_s below the scales.

2.3. Finite element micromechanical model

A two-dimensional plane strain composite scale-tissue micromechanical model was simulated using finite element analysis (FEA). The composite structure was discretized and modeled with quadratic continuum elements in ABAQUS/Standard (library types CPE6H and CPE8RH) and a fine mesh with elements of length $\sim t_s/4$ was needed to capture the deformation within the scales. Tissue and scale elements are modeled as perfectly bonded with properties found in Table 2. Non-linear, large deformation theory with frictionless contact between either a rigid plate or an indenter and the composite was assumed.

A blunt loading event was conducted in the form of a distributed compression of the scale assembly with a rigid plate. Simulations which consider the same finite length geometries and the same loading conditions as the experimental samples, were conducted and allow for direct comparison of model with experimental results. To simulate structures with many scales, such as those found on the entire length of a fish, periodic boundary conditions were also imposed on the lateral edges of the scale assembly while allowing overall expansion in the 1-direction (Fig. 3a). Further simulations were carried out changing the aspect ratio of the scales, $R_a = L_s/t_s$, from 50 to 100 by increasing the length of the scales L_s while holding scale volume fraction ϕ and angle θ fixed. This results in overlap K_d half of that shown in Table 1.

Macroscopic engineering stress and strain were calculated in the same manner as done experimentally (stress $\sigma = F_2/A$ and strain $\epsilon = \delta/H_{total}$). Local true Cauchy stress and logarithmic Hencky strain contours were evaluated at different load levels to identify the deformation mechanisms which accommodate the loading for the different composite geometries. For compressive loading, an effective secant stiffness $\overline{E}|_{\sigma = 0.05\ \mathrm{MPa}} = \sigma/\epsilon$ was determined and normalized by tissue elastic modulus E_t, highlighting the stiffness amplification effect of the scales. Angular rotation $d\theta$ of individual scales in response to loading was calculated with respect to initial angle: $d\theta = \theta' - \theta$ (Fig. 3). For small bending within an individual scale, the local deformed curvature is described by $\kappa = \partial^2 y'/\partial x'^2$ in a rotated coordinate frame (1′,2′) aligned with original scale angle θ. The average bending curvature along a scale of deformed length s is given by $\overline{\kappa} = 1/L_s \int_0^{L_s} \kappa\, ds$ and found by extracting the displacements u_1 and u_2 of nodes along the scale in the mesh.

Predatory attack via tooth indentation was simulated with rigid indenters of varying radii ($R/t_s = 0.1, 1, 10$) and a fixed half cone angle ($\theta/2$) of $\sim 30°$. Such finite radius indentation simulations are more representative of typical scale-tooth interactions. For these simulations, the thin epidermal tissue directly beneath the indenter was removed to account for the

highly localized aspects of deformation and to increase computational efficiency, as this thin outer layer of tissue would be pierced in a physiological setting. In addition, these indentations were performed on a very large sample (length $\gg L_s \cos\theta$) to neglect edge effects. For indentation, force is reported F_2 per unit width (plane strain) and indentation depth is normalized by sample height, δ/H_{total}. A normalized indentation force per depth (stiffness) is given by F_2H/δ_{tissue} and evaluated at $F=F_2=$ 5 N/mm.

3. Results and discussion

3.1. *Mechanical protection of finite-sized fish scale assembly under blunt loading*

The geometric arrangement of the scale and tissue structure governs the response to blunt loading, resulting in a substantial dependence of back deflection and stiffness on geometric arrangement of the assembly. Macroscopic loading curves for the finite-sized geometries are shown in Fig. 4(a) for three selected geometries (all with scale aspect ratio $R_a=50$): (i) $K_d=0.3$, $\theta=20°$, corresponding to $\phi=0.21$, (ii) $K_d=0.3$, $\theta=5°$, $\phi=0.77$, and (iii) $K_d=0.9$, $\theta=5°$, $\phi=0.26$. These particular geometries are highlighted because they demonstrate the functional effect of each structural parameter individually by sharing similar scale overlap K_d (i, ii), scale angle θ (ii, iii), or scale volume fraction ϕ (i, iii). The experimental and simulated loading curves for the same finite length geometries show that all structures studied have an initial non-linear response due to contact conditions from the irregular loading surface. It was also observed that the bilayer structure of the finite-sized composite allowed the bottom tissue layer of the samples to laterally expand significantly relative to the constrained expansion of the upper scale-tissue layer (seen in Fig. 5). This result is expected given the

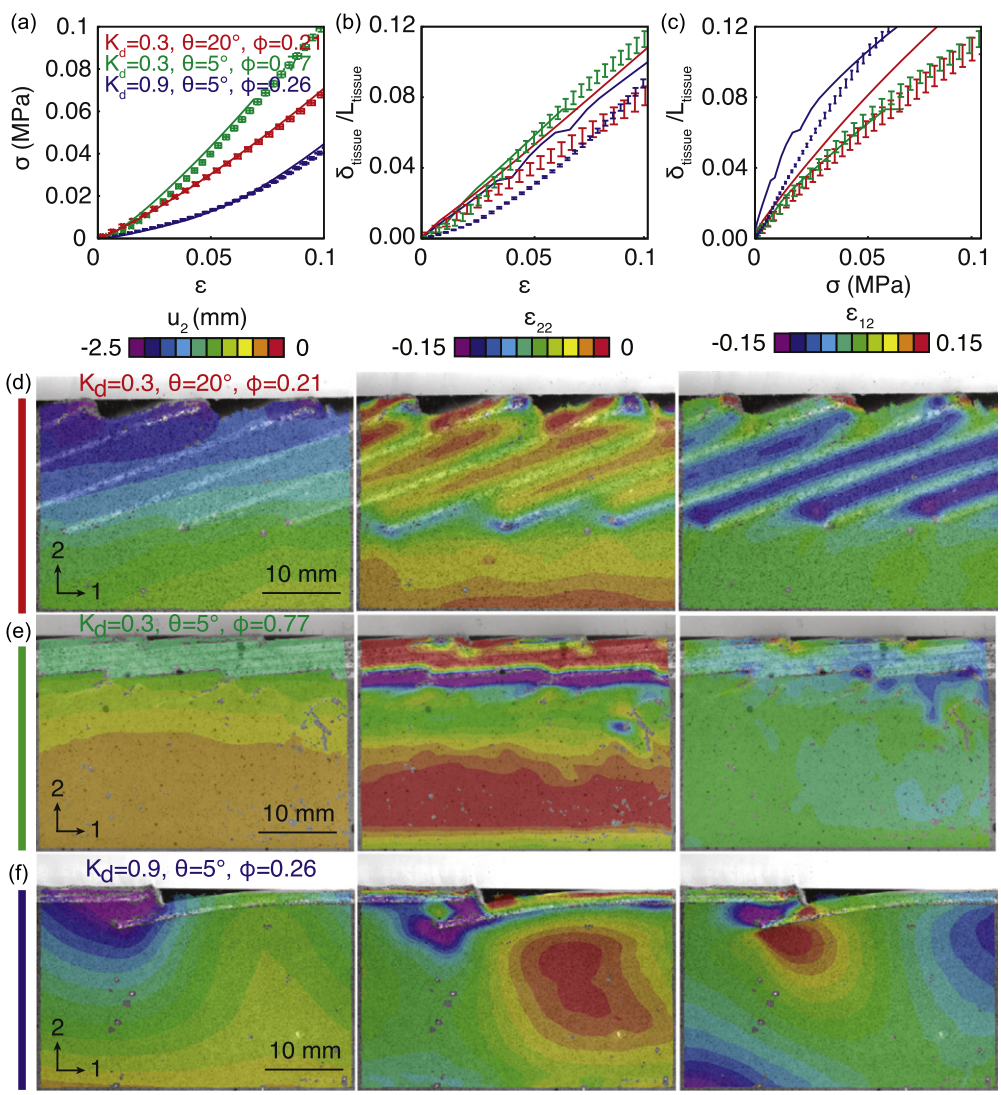

Fig. 4 – Effect of blunt loading on ABS and silicone rubber prototypes under plane strain compression for three selected geometries with $R_a=50$. (a) Corresponding experimental and simulation compression stress–strain curves, and back deflection as a function of (b) strain and (c) macroscopic stress. Error bars represent standard deviation of $n=3$ experiments and solid lines represent simulations of finite-sized geometry. (d–f) Selected experimental contours of displacement and strain are shown at macroscopic stress $\sigma=0.05$ MPa and indicate deformation within the composite structures.

additional stiffness of the composite layer (provided by the scales) constrains the lateral expansion of the tissue which leads to the barreling-like behavior observed in the bottom tissue layer, since the tissue near the interface with the upper scale-scale layer is constrained and that further away expands. For an infinitely periodic structure, the rubber cannot expand and is more fully constrained. This edge effect has a strong influence on several aspects of the results of the simulations, as discussed later in Section 3.2.1 where the influence of finite-sized specimens is compared to infinitely long periodic structures.

When evaluated at a fixed macroscopic strain, the effect of scale geometry on the maximum back deflection in the underlying tissue was found to be modest. As shown in Fig. 4b, increasing K_d from 0.9 to 0.3 (a ~3× increase in ϕ) offered a <10% decrease in back deflection δ_{tissue} at any fixed strain. However, the effective stiffness of the composites is strongly dependent on the scale arrangement, and hence, at a fixed macroscopic stress, the same ~3× increase in ϕ offers a 30–40% decrease in back deflection (Fig. 4c). Given that predatory attacks are often force-limited, these results show how geometric scale configurations and compositions observed in nature can protect underlying tissue by limiting tissue straining as expected. By tailoring the structural parameters, species are able to control the local protective function of their armors.

Experimental contours of displacement and strain agree well (Figs. 4 and 5) with simulated results of the same geometry, demonstrating the quantitative capabilities of the model and providing insights into the deformation mechanisms. Depending on the geometric arrangements and volume fractions of the scales, macroscopic loading is accommodated by either (1) global tissue shear between scales and scale rotation, (2) local tissue shear at scale tips and scale bending, or (3) constraint of the tissue and overall stiffening. These deformation mechanisms are illustrated using the three selected geometries in Figs. 4 and 5.

Tissue shear and scale rotation. As shown in the contours of Fig. 4(d) for K_d=0.3, $\theta=20^\circ$, the anisotropy from the angled scales couples the compressive loading to a shear strain ϵ_{12} within the tissue. For similar architectures with high scale overlap (low K_d) and initial angle θ, this region of shear strain is broad and evenly distributed over the length of the scales. This mechanism of shear between scales promotes uniform scale rotation, as shown in Figs. 4(d) and 5(a). Here, the scales deform minimally as they rotate relative to the tissue; deformation is accommodated through tissue shearing. This effect was largely observed for structures with $\theta>20^\circ$. Experimental results capture this effect well with the exception of geometries with ϕ~1, in which the imaging pattern could not resolve the very narrow tissue layer between scales (Fig. 4e).

Scale bending. Upon blunt loading, it can be seen in Fig. 4(f) that the scales in the arrangement with K_d=0.9, $\theta=5^\circ$ have noticeably deformed from their original configuration (Fig. 2). Here, the scales locally bend to accommodate the loading, resulting in highly localized shear strain in the regions of scale overlap. Such low overlap results in undesirable localized regions of strain in the tissue substrate, shown in the contours of ϵ_{22} and ϵ_{12}. Due to the small feature size and non-linear deformation of the scales during bending, digital image correlation was not able to fully capture the motion of the scales. It can also be seen for other architectures with $K_d>0.5$ that the scales with low overlap underwent significant local bending, often constrained by three or more points of inflection.

Tissue constraint. The scale layers imposed a significant constraint on the underlying tissue, constraining lateral expansion. This constraint is apparent in the deformed images of Fig. 5, which shows the constrained bulging of the underlying tissue in the finite strained samples. This constraint effect will be shown to provide significant stiffening and hence dramatic reduction in back deflection of the overall composites when evaluating the periodic structure.

Loading curves from experiments on physical prototypes agree well (Fig. 4a) with simulations of the same geometry and display the behavior of the composite structure. A secant stiffness was extracted from loading curves at a fixed macroscopic stress of σ=0.05 MPa (corresponding to $\epsilon=0.02-0.17$) and was found to range from $\overline{E}=$ 1–3 across the geometries studied (Fig. 6a). This secant stiffness captures the effective "springs in series"-like stiffness of the tissue support layer and the scaled layer. Assemblies with a low volume fraction of scales had $\overline{E}\sim E_t$; indirectly, these low volume fraction scale assemblies do not limit back deflection. Increasing ϕ from 0 to 0.25 promotes a nearly linear increase in $\overline{E}$ from 1 to 2 and further increasing ϕ gives a plateau of $\overline{E}=3$ at $\phi=0.5$. These results show the effect of increasing ϕ on limiting back deflection and suggest a plateau of influence at $\phi=0.5$. While effective stiffness of the composite is one indicator of the protective response of the system, it does not explicitly

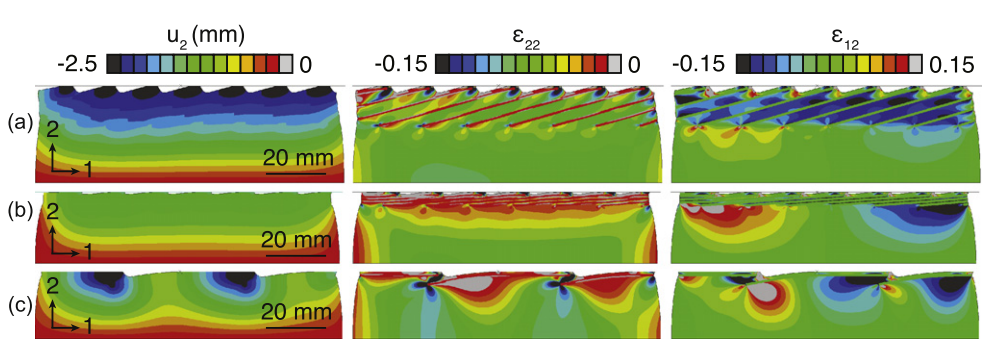

Fig. 5 – Simulated contours of displacement and strain are shown at macroscopic stress $\sigma=0.05$ MPa corresponding to experiments of blunt loading of physical models in Fig. 4. The bottom tissue layer is shown to laterally bulge relative to the upper scale-tissue layer. Similar results were observed experimentally (not shown). (a) K_d=0.3, $\theta=20$ deg, corresponding to ϕ=0.21, (b) K_d=0.3, $\theta=5$ deg, ϕ=0.77 and (c) K_d=0.9, $\theta=5$ deg, ϕ=0.26.

describe the effects experienced in the underlying tissue. To function as an effective dermal armor, fish scales must minimize the deflections, strains and/or stresses beneath the scale layer to protect the body. Experimental results show that back deflection in the underlying tissue, δ_{tissue}, decreases as scale volume fraction increases for $\phi<0.5$ and then remains at $\delta_{tissue}/L_{tissue}\sim 0.04$ for $\phi>0.5$ (Fig. 6b).

3.2. *Mechanical protection of infinitely long (periodic) fish scale assembly under blunt loading*

3.2.1. *Deformation mechanisms in periodic structures*

Since the actual structures consist of many repeating scales along the length of the fish body, simulations with periodic boundary conditions which capture an infinitely long structure provide a more physiologically relevant assessment of the mechanical response than the simulations of the finite-sized specimens. Recall the finite-sized specimens exhibited significant lateral expansion (bulging) of the bottom soft tissue substrate (Fig. 5) due to the unconstrained lateral edges. The relaxed boundary conditions in these finite-sized specimens cause the structures to exhibit a more compliant response. In an infinitely periodic structure, the lateral strain of both layers must be identical based on the compatibility. The implications of this constraint have a dramatic impact on tissue deformation for geometries with stiff upper scale-tissue layers, in which the expansion of the lower layer is constrained by the presence of and compatibility with the scale layer. To eliminate these boundary effects, a periodic structure was simulated to more accurately model a larger number of repeating scales along the length, such as those found along the length of a fish body.

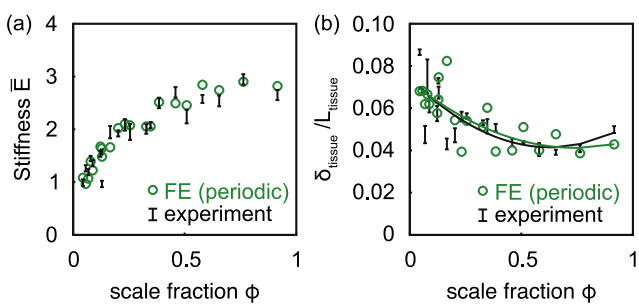

Fig. 6 – Experimental and finite sized simulation results for 21 total geometries with $R_a=50$. (a) Stiffness and (b) back deflection in response to blunt loading are evaluated at $\sigma=0.05$ MPa.

The resulting loading curves and contours for the periodic structure are shown in Fig. 7, which demonstrate the large difference the constraint from periodicity has on the results for geometries with high ϕ. Imposing periodic boundary conditions has little effect for small volume fraction ($\phi<0.2$), but as ϕ increases, the effective stiffness of the periodic scale structure increases by an order of magnitude over the finite length structures, which had permitted lateral deformation (bulging) of the underlying tissue. The effective stiffness of the periodic structure follows a nearly linear relationship with scale fraction ϕ (Fig. 9(a)) and shows the direct effect that increasing scale armor has on limiting back deflection at a given macroscopic stress level (Fig. 9(b)). This relationship between back deflection and scale volume fraction demonstrates that the volume fraction of scales governs the constraint of the tissue layer and in turn, has a significant influence on protection. Therefore, effective stiffness and back deflection can be adjusted by tailoring the scale fraction $\phi(K_d,\theta)$.

One aspect of the constraint effect of increased ϕ on effective stiffness is demonstrated in the geometry of Fig. 7(c), which has the same overlap as Fig. 7(b) but a significantly higher scale volume fraction, which was achieved by reducing the angle of the scales from 20° to 5°, resulting in a stiffer loading curve and far less penetration in the underlying tissue (u_2,δ_{tissue}) at a given force. In this case, by reconfiguring the angle of the same number of scales in a cross section (K_d^{-1}), the system can achieve a 4× increase in penetration resistance. These results show how the geometric arrangement of the scales and the scale volume fraction, together with their influence on constraining the deformation of the underlying tissue, serve to provide protection. Furthermore, such scale-imposed tissue constraint could serve as a design principle for these composite structures to locally tailor stiffness.

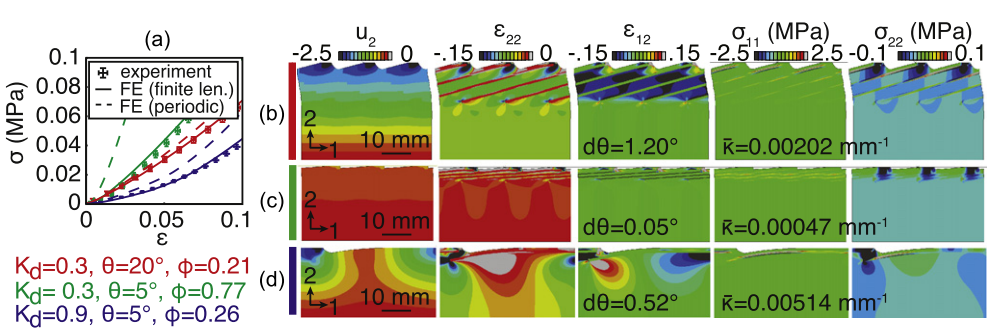

Fig. 7 – Periodic simulations for $R_a=50$ yield insights into deformation mechanisms of periodic scale assembly under blunt loading. (a) Loading curves demonstrate stiffening constraint for structures with high ϕ. Contours are evaluated at $\sigma=0.05$ MPa, (b) large initial scale θ promotes rotation of scales via uniform tissue shearing (ϵ_{12}), (c) high scale volume fraction directly results in a stiff composite, which reduces back deflection in the underlying tissue u_2 and (d) geometries with little scale overlap (high K_d) exhibit excessive scale bending (σ_{11}) and localized high stress (σ_{22}) and strain in the underlying tissue.

The underlying deformation mechanisms for the structures with periodic boundary conditions were also identified. Similar to results from finite-sized geometry, scale bending, scale rotation, and tissue shear were found to be the primary modes of deformation. The mechanisms of scale bending and rotation are dependent on initial overlap (K_d) and angle (θ) (Fig. 9). Architectures with low overlap (high $K_d \sim 1$) are dominated by scale bending, while those with high initial angle θ are dominated by tissue shearing and corresponding scale rotation. This behavior is demonstrated by the high values of contours of bending stress (σ_{11}) found within the minimally overlapping scales in Fig. 7(d) for a macroscopic stress of $\sigma = 0.05$ MPa. Scales in such configurations at this load have an effective curvature of $\overline{\kappa} > 0.25 L_s^{-1}$, or equivalently, an effective bending radius of $\overline{R} < 4L_s$. Conversely, the large initial angle θ in Fig. 7(b) results in a shear straining (ϵ_{12}) of the tissue, which in turn, leads to the rotation of the scales. Structures with both high K_d and θ (corresponding to $\phi < 0.1$) exhibit both significant scale bending and scale rotation, but such configurations are typically not observed in nature.

3.2.2. *Work of deformation*

To determine the ideal armor architecture under blunt loading, the deformation resistance of the composite must be evaluated against competing mechanical functionalities. Given that the stiffness of structures ($\overline{E}$) and their work of deformation (W) are inversely related when evaluated at a fixed load, it is problematic to select a structure that combines both high stiffness and high work of deformation. Thus, if both properties of high $\overline{E}$ and W are desired, an intermediate value of ϕ must be selected to balance these two criteria.

3.2.3. *Effect of scale morphometry*

Increasing the aspect ratio of scales $R_a = L_s/t_s$ from 50 to 100 was performed in three ways: (a) fixing ϕ,θ and varying K_d, (b) fixing K_d,θ and varying ϕ, and (c) fixing ϕ,K_d and varying θ. The resulting geometries, stress–strain curves, and contours of σ_{22} are shown in Fig. 8. To compare the same composition and contact geometry of varying architectures, scale volume fraction ϕ and angle θ were held constant and evaluated for all geometries as a function of $\phi(K_d,\theta,R_a = 100)$. This combination of parameters is reflected in Fig. 8(b), while Fig. 8(a) shows the original structure from the previous discussion.

Here for the same volume fraction of scales ϕ and a given fixed θ, the increase of aspect ratio reveals a tradeoff between dominant deformation mechanisms. Increasing the aspect ratio via reducing K_d increases the effective stiffness $\overline{E}$ of the assemblies, resulting in a reduced back deflection in the underlying tissue (Fig. 9). To examine the mechanics that govern this response, scale bending $d\theta$ and rotation $\overline{\kappa}$ were evaluated for the infinitely periodic case. Bending within the scales was reduced for higher aspect ratio simulations, which is explained by the corresponding decrease in scale overlap. However, the trend in Fig. 9(c) suggests that scale with the same overlap K_d and increased aspect ratio would bend much more than those with the original aspect ratio, showing the large influence of R_a on the local deflections and bending curvature of the scales. Despite the same fraction of tissue in the composite, shearing of the tissue was notably reduced. Hence, while scale bending increased, scale rotation was found to significantly decrease. This is noteworthy because previous results suggest scale angle θ (here, fixed) governs tissue shear and scale rotation. This transition from tissue shear plus scale rotation to scale bending with increasing aspect ratio served to stiffen the composite, yet resulted in elevated levels of local bending stress within the scales. These higher bending stresses will lead to early failure of the scales via yielding or fracture.

Alternatively, the aspect ratio of the scales can be increased by fixing the scale volume fraction ϕ and the scale overlap K_d and varying the scale angle θ. Changing the fixed parameters results in a completely different structural arrangement, as shown in Fig. 8(d). This structure with fixed ϕ,K_d,R_a results in both more bending and rotation than the original structure, yet is less stiff. These results further suggest that aspect ratio alone cannot govern the deformation mechanisms of the structure and that the response is a function of composition (ϕ), structural arrangement (K_d,θ) and morphometry (R_a).

In general, the morphometry of the scales helps to govern the dominant deformation mechanism of the assembly, but is dependent on the spatial arrangement of the scales. Typically, thin, high aspect ratio scales result in deformations primarily dominated by bending, whereas thick (low aspect ratio) scales are dominated by tissue shear plus scale rotation. This tradeoff can be tailored by adjusting individual

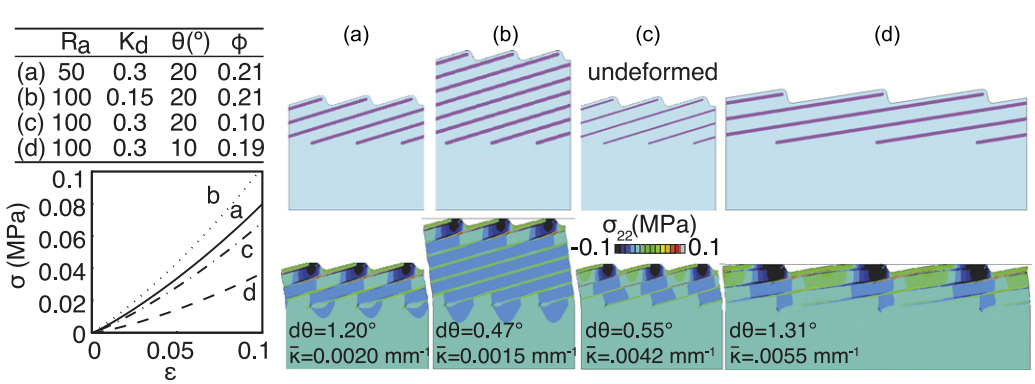

Fig. 8 – Effect of scale morphometry. Increasing scale aspect ratio $R_a = L_s/t_s$ from 50 to 100 as a function of varying K_d, θ, ϕ. Stress–strain curves and contours of σ_{22} are shown for these combinations of geometric parameters. Architecture in (a) is used in Section 3.2.1 and (b) in Section 3.2.3.

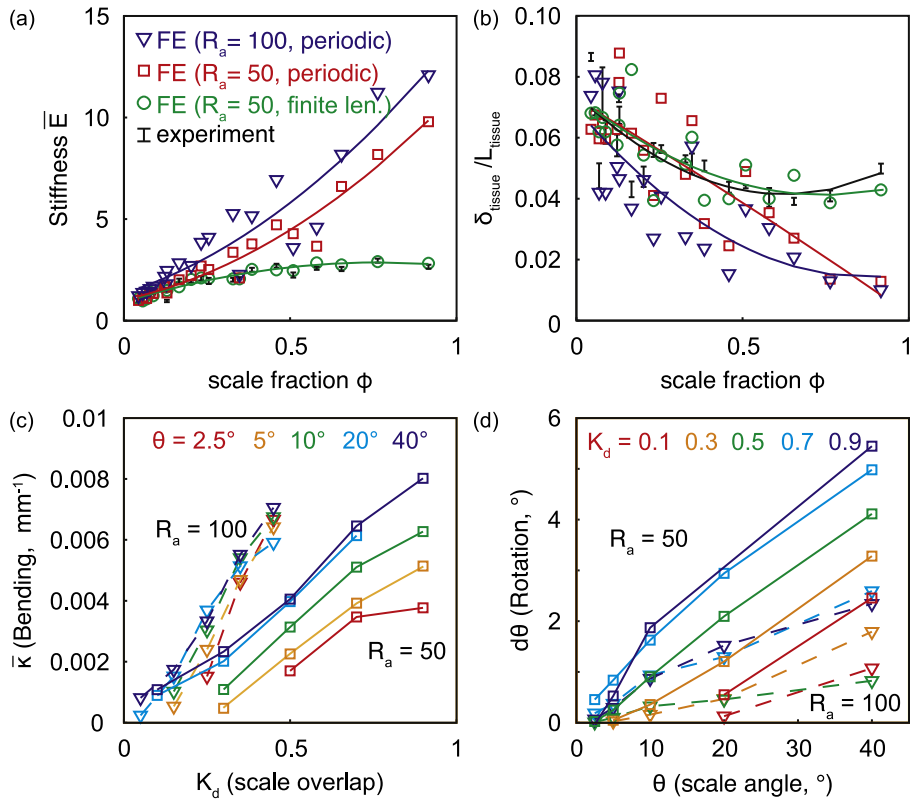

Fig. 9 – Deformation mechanisms for uniform compression evaluated at a macroscopic stress of $\sigma = 0.05$ MPa for 21 total geometries with $R_a = 50$ and 100. (a) For low scale volume fractions ($\phi < 0.25$) in experiments and finite length simulations, effective loading stiffness $\bar{E}$ of the composite increases linearly with scale fraction then plateaus for $\phi > 0.5$. Similarly, back deflection in the underlying tissue, δ_{tissue}, decreases linearly for $\phi < 0.5$. Periodic simulations suggest that this plateau for large ϕ is a boundary effect. For periodic simulations, (c) microscopic scale bending is primarily a function of overlap K_d, where as (d) scale rotation is dependent on initial scale θ. Transition from rotation to bending is evident for large R_a (dashed line).

scale aspect ratios in addition to other properties, e.g. elastic modulus, internal structure, and porosity of the scales.

3.3. *Mechanical protection of fish scale assembly under predatory tooth attack*

While blunt loading predicts the behavior of the assembly to large indenters ($R \gg K_d L_s$), threats are often localized to a small area. Idealizing predatory biting as a sharp tooth of radius R, the corresponding contact area and the resulting deformation-induced scale-tissue interactions govern the number of scales that are involved in the deformation. For physiologically relevant indentation ($R < K_d L_s$), the indenter only comes into direct contact with one scale. Underlapped and adjacent scales are also deformed, as governed by K_d. Under low penetration loads, the scales are not locally indented, but rather undergo significant bending with the compliant tissue between the scales shearing and the tissue beneath the scales also shearing (Fig. 10). For the case of a conical rigid indenter tip at low loads ($F = 5$ N/mm), there is a single point of contact and the resulting loading curves and underlying tissue deformation were found to be nearly identical for the range of $R/t_s = 0.1, 1, 10$ simulated. Note that this force of $F = 5$ N/mm is only relevant for the materials properties and scale size shown in Table 2 where $R_a = 50$ and $H_{tissue} = L_s/2$.

The similarity of both the loading curves and the back deflection corresponding to $K_d = 0.3$, $\theta = 20°$, $\phi = 0.21$, and $K_d = 0.3$, $\theta = 5°$, $\phi = 0.77$ indicates that the common overlap of $K_d = 0.3$ controls the mechanical response of the composite. In contrast, the response for $K_d = 0.9$, $\theta = 5°$, $\phi = 0.26$ is much more compliant and permits more back deflection δ_{tissue} in the underlying tissue because of the minimally overlapping scales of $K_d = 0.9$. Localized indentations of $R/t_s = 0.1$ are primarily accommodated through the mechanism of scale bending, which is isolated to only a few scales. Evaluating across all architectures $\phi(K_d, \theta)$, the overlap of the scales (K_d) governs the ability of the composite to resist penetration (Fig. 11). Normalized indention force (local stiffness) increases with increasing scale overlap (decreasing K_d). Similarly, back deflection in the underlying tissue was found to decrease with overlap such that architectures with highly overlapping scales ($K_d \sim 0$) are very stiff and had minimal back deflection. Due to the localized, non-uniform deformation of the assembly under finite indentation, scale rotation is no longer a dominant deformation mechanism. In these layered composite structures, the overlap, angle, and volume fraction work together to give interplay between scale bending and shearing of the tissue to involve more material. These geometries are mechanisms for increasing work of deformation by involving greater amount of material laterally as well as to deeper depths.

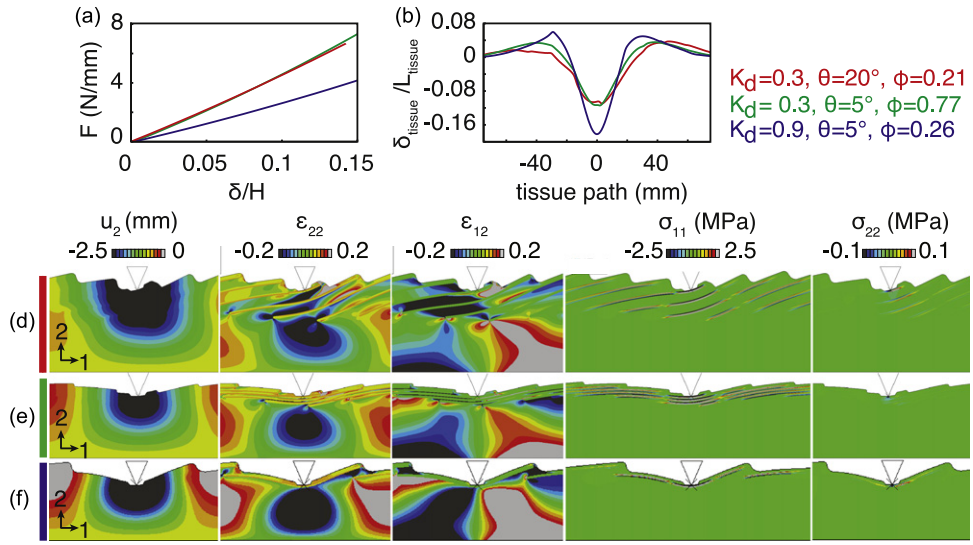

Fig. 10 – Indentation on fish scale assembly for radius $R/t_s = 0.1$. (a) Loading curves for three geometries show that indentation force is nearly identical for architectures with similar overlap, despite very different θ, ϕ and (b) corresponding underlying back deflection and (d–f) contours of stress, strain taken at $F = 5$ N/mm.

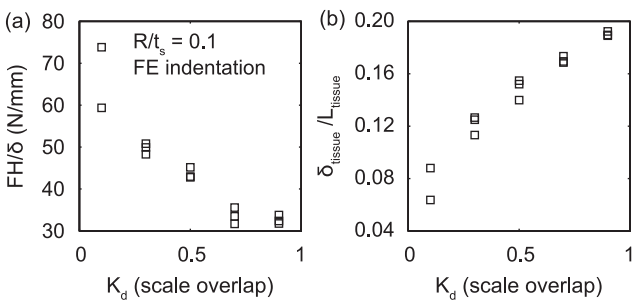

Fig. 11 – Indentation force and back deflection evaluated at $F = 5$ N/mm across all scale assembly architectures $\phi(K_d, \theta, R_a = 50)$ for a sharp indenter with radius $R/t_s = 0.1$. Overlap K_d governs the ability of the composite to resist penetration, which is dominated by the deformation mechanism of scale bending.

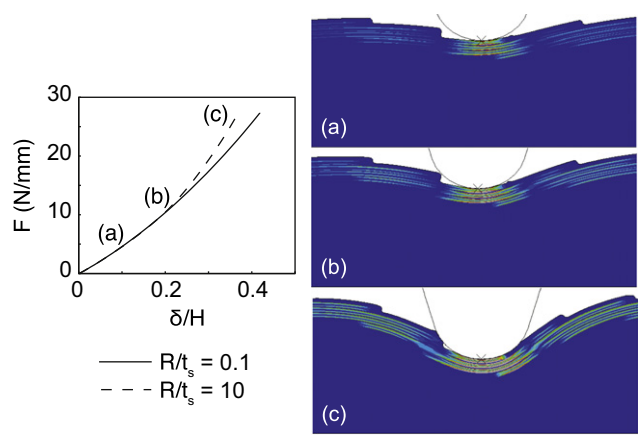

Fig. 12 – Indentation loading curves for varying indenter geometry ($R/t_s = 0.1, 10$) show little effect of R on mechanical response due to point-wise interaction for small loading. At larger loads, the scale deforms around the indenter radius and the reaction force increases. Contours shown of $\bar{\sigma}$ for geometry with $K_d = 0.3$, $\theta = 5$ deg, $\phi = 0.77$.

Larger indenters ($R > K_d L_s$ and simulated for $R/t_s = 10$ as shown in Fig. 12) under large penetration loads permit the scale to bend around the indenter. Above $F = 10$ N/mm, these larger radius indenters produce a stiffer behavior as the contact area between scale and tooth increases. For indenters whose radii span multiple scales, the load is distributed across the scale assembly which reduces deflections, scale deformation, and stress concentrations, thereby protecting the fish. This explains why predators benefit from having sharper teeth: by localizing the biting force to a small contact area, the local contact stresses are increased. This effect is compounded for segmented systems such as fish scales, whereby if one scale sees too much bending, the scale and subsequently the entire assembly can be defeated. Sharper radius teeth permit predators with a given biting force to isolate a single scale and penetrate the underlying tissue. By localizing the indentation deformation to a finite region, predators with a given biting force are able to penetrate the underlying tissue. While this elastic model does not incorporate failure mechanisms such as fracture, delamination, or plasticity, the stress distributions within the scales and tissue give insight to failure modes and locations resulting from excessive deformation. High shear strain ϵ_{12} of the tissue promotes failure by delamination of the tissue-scale interface, which permits scales to dislodge and damage the structure of the composite. Alternatively, regions of high bending stress σ_{11} of the scale promote yield and fracture of the scale.

4. Conclusions

Fish scale armor provides a model biomimetic composite for the design of structures to provide global penetration

resistance and flexibility. Biological systems have a limited library of materials available, often consisting of rigid mineralized components and compliant organic tissues. The morphology and architecture of the material organization is one unique way to provide a spectrum of structural functionalities. Overlapping scale units distribute stresses across a large volume of material and provide penetration resistance at a reduced weight (and subsequent cost of mineralization) compared to a continuous armor layer. Scale architecture (K_d, θ), composition (ϕ), and morphometry (R_a) can be used to locally tailor composite stiffness and back deflection in the underlying tissue in order to achieve protection. The flexibility of the scales and tissue permits the scales to rotate and bend under applied loading. Assemblies of these scaled structures are formed without joints or hinges, forming a simple, easily adaptable design. The degree of flexibility or protection is reconfigurable by simply changing morphometry and the overlap distribution of the scales.

Under blunt loading, the composition primarily governs the effective response of the composite, which is achieved by a combination of deformation mechanisms controlled by the microstructural arrangement. Inclusion of a compliant tissue is key to understanding the true behavior of the composite, which is dominated by tissue constraint, tissue shearing (and resulting scale rotation), and scale bending. Volume fraction ϕ governs constraint, effective stiffness, and back deflection; scale overlap K_d governs scale bending, and initial scale angle θ governs tissue shearing and scale rotation. The influence of these mechanisms can be tailored by adjusting the scale morphometry: for scales with a large aspect ratio, the deformation mechanisms will be dominated by scale bending. Conversely, scales with small aspect ratio will rotate under blunt loading, accommodated by tissue shearing.

As the contact area of the loading surface is reduced to a finite radius penetration indentation, there is a transition from tissue constraint and scale rotation to a deformation dominated by localized scale bending, which is accommodated by shearing of the tissue interlayers and the underlying tissue substrate and governed by the overlap of the scales. Architectures with high scale overlap (low K_d) resist penetration by distributing loading over a large area. Deformation of a scale during localized bending could risk failure by plastic deformation or fracture, exposing the underlying tissue and defeating the armor. Here, highly overlapping scales are beneficial as they provide multiple layers of defense; in order to penetrate the tissue, the indenter must deform and defeat K_d^{-1} scales. Alternatively, while scale rotation risks injury to the compliant tissue by delaminatation or tearing, the stiff scale protective layer remains intact. Such mechanical characterization could have useful applications in developing principles for protective systems (Neal and Bain, 2004), composite textiles (Hatjasalo and Rinko, 2006), and even electronics (Kim et al., 2012).

Acknowledgments

This research was supported by the U.S. Army Research Office through the MIT Institute for Soldier Nanotechnologies under contract W911NF-07-D-0004 and Institute for Collaborative Biotechnologies (ICB) under contract DAAD-19-02-D0002.

Appendix A. Supplementary data

Supplementary data associated with this article can be found in the online version at http://dx.doi.org/10.1016/j.jmbbm.2012.11.003.

REFERENCES

Arciszewski, T., Cornell, J., 2006. Bio-inspiration: learning creative design principia. In: Smith, I. (Ed.), Intelligent Computing in Engineering and Architecture. Springer, Berlin, Germany. pp. 32–53.

Burdak, V.D., 1979. Morphologie fonctionnelle du tégument écailleux des poissons. Kiev: La Pensée Scientifique (in Russian). French translation, Cybium 10, 1986, 1–147.

Colbert, E.H., Morales, M., 2001. Colbert's Evolution of the Vertebrates: A History of the Backboned Animals Through Time. Wiley-Liss.

Connors, M.J., Ehrlich, H., Hog, M., Godeffroy, C., Araya, S., Kallai, I., Gazit, D., Boyce, M.C., Ortiz, C., 2012. Three-dimensional structure of the shell plate assembly of the chiton Tonicella marmorea and its biomechanical consequences. Journal of Structural Biology 177, 314–328.

Francis, R., 1990. Back-calculation of fish length: a critical review. Journal of Fish Biology 36, 883–902.

Garrano, A.M.C., Rosa, G.L., Zhang, D., Niu, L.N., Tay, F., Majd, H., Arola, D., 2012. On the mechanical behavior of scales from Cyprinus carpio. Journal of the Mechanical Behavior of Biomedical Materials 7, 17–29.

Gemballa, S., Bartsch, P., 2002. Architecture of the integument in lower teleostomes: functional morphology and evolutionary implications. Journal of Morphology 253, 290–309.

Guinan, M.J., Anatomy 100: Integument, University of California at Davis Lecture. 〈http://guppiesonli.wordpress.com/guppy-articles/skin-structure-of-guppy/〉. Last accessed May 1, 2012.

Hatjasalo, L., Rinko, K., 2006. Elastic composite structure. US Patent 7153789.

Hawkes, J., 1974. Structure of fish skin 1: general organization. Cell and Tissue Research 149, 147–158.

Hebrank, M.R., Hebrank, J.H., 1986. The mechanics of fish skin: lack of an external tendon role in two teleosts. The Biological Bulletin 171, 236.

Ibanez, A., Cowx, I., O'Higgins, P., 2009. Variation in elasmoid fish scale patterns is informative with regard to taxon and swimming mode. Zoological Journal of the Linnean Society 155, 834–844.

Ikoma, T., Kobayashi, H., Tanaka, J., Walsh, D., Mann, S., 2003. Microstructure, mechanical, and biomimetic properties of fish scales from Pagrus major. Journal of Structural Biology 142, 327–333.

Jawad, L., Al-Jufaili, S., 2007. Scale morphology of greater lizardfish *Saurida tumbil* (Bloch, 1795)(Pisces: Synodontidae). Journal of Fish Biology 70, 1185–1212.

Kim, S., Su, Y., Mihi, A., Lee, S., Liu, Z., Bhandakkar, T.K., Wu, J., Geddes III, J.B., Johnson, H.T., Zhang, Y., Park, J.K., Braun, P.V., Huang, Y., Rogers, J.A., 2012. Imbricate scales as a design construct for microsystem technologies. Small 8, 901–906.

Lin, Y.S., Wei, C.T., Olevsky, E.A., Meyers, M.A., 2011. Mechanical properties and the laminate structure of *Arapaima gigas* scales. Journal of the Mechanical Behavior of Biomedical Materials 4, 1145–1156.

Meyers, M., Lin, Y.S., Olevsky, E.A., Chen, P.Y., 2012. Battle in the Amazon: Arapaima vs. Piranha. Advanced Engineering Materials 14, B279–B288.

Neal, M.L., Bain, A.D., 2004. Method and apparatus for defeating ballistic projectiles. US Patent 6745661.

Park, E., Lee, S., 1988. Scale growth and squamation chronology for the laboratory-reared hermaphroditic fish *Rivulus marmoratus* (Cyprinodontidae). Japanese Journal of Ichthyology 34, 476–482.

Sire, J., 1990. From ganoid to elasmoid scales in the actinopterygian fishes. Netherlands Journal of Zoology 40, 75–92.

Sire, J.Y., Donoghue, P.C.J., Vickaryous, M.K., 2009. Origin and evolution of the integumentary skeleton in non-tetrapod vertebrates. Journal of Anatomy 214, 409–440.

Song, J., Reichert, S., Kallai, I., Gazit, D., Wund, M., Boyce, M.C., Ortiz, C., 2010. Quantitative microstructural studies of the armor of the marine threespine stickleback (*Gasterosteus aculeatus*). Journal of Structural Biology 171, 318–331.

Torres, F.G., Troncoso, O.P., Nakamatsu, J., Grande, C.J., Gomez, C.M., 2008. Characterization of the nanocomposite laminate structure occurring in fish scales from *Arapaima gigas*. Materials Science and Engineering C: Materials for Biological Applications 28, 1276–1283.

United States Fish and Wildlife Service, 2010. Normal trout histology. http://training.fws.gov/ec/fish/histo1.html. Last accessed May 1, 2012.

Vernerey, F.J., Barthelat, F., 2010. On the mechanics of fishscale structures. International Journal of Solids and Structures 47, 2268–2275.

Whitear, M., 1986. The skin of fishes including cyclostomes: epidermis. In: Bereiter-Hahn, J., Matoltsy, A., Richards, K. (Eds.), Biology of the Integument. Springer, Berlin, Germany. pp. 8–38.

Whitenack, L.B., Simkins Jr., D.C., Motta, P.J., 2010. Biology meets engineering: the structural mechanics of fossil and extant shark teeth. Journal of Morphology 272, 169–179.

Zhu, D., Ortega, C.F., Motamedi, R., Szewciw, L., Vernerey, F., Barthelat, F., 2012. Structure and mechanical performance of a modern fish scale. Advanced Engineering Materials 14, B185–B194.